

# Optical modeling for a two-stage parabolic trough concentrating photovoltaic/thermal system using spectral beam splitting technology

Shouli Jiang, Peng Hu <sup>\*</sup>, Songping Mo, Zeshao Chen

Department of Thermal Science and Energy Engineering, University of Science and Technology of China, 96 Jinzhai Road, Hefei 230027, Anhui, PR China

## ARTICLE INFO

### Article history:

Received 23 April 2009

Accepted 10 May 2010

### Keywords:

Solar energy

Power generation system

Parabolic trough collector

Optical modeling

Beam splitting filter

## ABSTRACT

A two-stage parabolic trough concentrating photovoltaic/thermal (PV/T) system is described, which contains a concentrator, a spectral beam splitting filter, an evacuated collector tube and the solar cell components. The nondimensional optical model with the focal length of the concentrator as the characteristic length has been developed to analyze the properties of the concentrating system using the beam splitting filter. The geometry concentration ratio and the size of solar image at different structure parameters have been obtained. Based on the ray tracing algorithms, a detailed three-dimensional model is set up to evaluate the local radiation flux density distribution on the elements' surfaces. And the effects of the solar brightness distribution and optical errors (e.g., alignment error and tracking error) are also involved. Furthermore, the spectral distribution of the solar radiation is illustrated with the beam splitting filter, which has been specially designed using the needle optimization method. It is shown that using the filter the heat load of the cell can be reduced by 20.7%, up to 10.5% of the total incident solar energy can be recovery by the receiver, and the overall optical efficiency in theory is about 0.764.

© 2010 Elsevier B.V. All rights reserved.

## 1. Introduction

One of the suggested effective approaches to reduce the amount of the expensive photovoltaic cell is concentrating incident sunlight using cheaper optical components [1,2]. The higher the concentration ratio level is, the less the cell area required is. But high concentration system is not always cost-effective for the more expensive concentrator solar cell employed. So the low-concentration-ratio solar system with conventional silicon flat panel solar cells is surveyed.

The concentrating PV system will be more competitive in price with the panel PV system by increasing concentration ratio level, whereas the photovoltaic conversion efficiency degrades as the solar cell temperature rises up in view that waste heat cannot be dissipated in time [3,4]. An option is to use spectral beam splitting technology to reduce the heat load on the solar cell and to increase the concentration ratio as well as the system efficiency [5,6]. An example is the case of the two-stage parabolic trough concentrating beam splitting PV/T (TTCSPV/T) system proposed by Chen et al. [7]. It is a linear parabolic system with two parabolic mirrors and a tubular receiver for heat recovery, whose concept is presented in Fig. 1. The primary concentrator mirror is

usually coated with aluminum or silver [8,9]. And the secondary mirror surface is specially deposited a wide spectrally selective coating, of which the ideal spectral reflectivity is suggested as

$$\rho(\lambda) = 0 \quad \text{for } \lambda \geq \hbar c/E_g \quad (1a)$$

$$\rho(\lambda) = 1 \quad \text{for } \lambda < \hbar c/E_g \quad (1b)$$

where  $\hbar$  is Planck's constant,  $E_g$  is the band-gap of the solar cell and  $c$  is the speed of light in vacuum. It is a complex multilayer film stack with a high transmittance for the photons below the band-gap to be ultimately absorbed by the tubular receiver and the other photons are reflected onto the cell.

The TTCSPV/T hybrid system aims to increase the overall efficiency of solar utilization by PV conversion and medium temperature power generation. So it is very important to evaluate the optical properties of the concentrating system. The model is to be used for discussing the geometric concentration ratio, the spacial and spectral distribution of the solar irradiance density. Hence, the simple two-dimensional geometrical optical model is presented. There are a number of prior studies of optical simulation models for concentrating systems (e.g., [10–13]). The ray tracing method in the dimensionless form is employed to evaluate the local irradiation flux density. It is a detailed 3D analysis model using a quick and accurate numerical algorithm, and the effect of solar brightness distribution is analyzed, as well as of the optical errors, including tracking error and alignment

<sup>\*</sup> Corresponding author. Tel.: +86 551 3601656; fax: +86 551 3606459.  
E-mail address: [Hupeng@ustc.edu.cn](mailto:Hupeng@ustc.edu.cn) (P. Hu).

Nomenclature	Greek symbols
$A(a)$ aperture of parabolic mirror, mm	$\alpha$ circumferential angle of incident rays in beam cone
$B$ intercept of sunlight rays	$\beta$ radial angle of incident rays in beam cone, mrad
$CR$ geometric concentration ratio of TTCSPV/T	$\gamma, \theta$ tracking parameters in the mathematical model
$d_{\text{Sun}}$ diameter of the Sun, m	$\gamma_{\text{De}}, \gamma_{\text{RA}}$ angles of the two-axis tracking unit
$D(d)$ diameter of heat receiver tube, mm	$\delta$ solar intercept angle, mrad
$e$ solar energy of ray, W	$\eta_0$ overall optical efficiency
$E$ radiant intensity, W/m <sup>2</sup>	$\theta_0$ half intercept angle of the sun, mrad
$F(f)$ focus length of parabolic mirror, mm	$\kappa, \mu$ variables of the solar brightness distribution
$K$ rate of grade of sunlight rays	$\lambda$ wavelength, nm
$K_1$ rate of grade of incident sunlight rays	$\xi$ local relative irradiation flux density
$K_2$ rate of grade of primary reflection rays	$\rho$ reflectance of optical element
$K_3$ rate of grade of secondary reflection rays	$\sigma$ standard deviation of the evaluation results
$L(l)$ length of parabolic trough, mm	$\phi$ distribution function of solar brightness
$L_0$ distance between the Earth and the Sun, m	$\varphi_{\text{rim}}$ rim angle of parabolic collector, deg
$\mathbf{n}(n)$ vector (component of vector) of rays	$\chi$ circumsolar ratio, CSR
$N$ number of calculation grid or sunlight ray	
$N_{\text{Day}}$ the day of the year	
$t$ parameter of ray equation	
$T$ transmissivity	
$W(w)$ width of solar cell, mm	
$Z_{R0}$ center point of the receiver tube on focus axis	
$Z_{S0}$ base point of the beam filter on focus axis	
$\Delta Z_{R0}$ receiver alignment error on Z-axis	
$\Delta Z_{S0}$ splitting filter alignment error on Z-axis	
	<b>Subscripts</b>
	C parabolic trough collector
	$i, j, k$ mark number of calculation grid
	P incident point on optical element
	R receiver tube
	S spectral beam splitting filter
	SC solar cell
	SD solar disk

error. The spectral model is set up to analyze the spectral distribution of the solar energy in the TTCSPV/T system.

## 2. Physical model

As far as the TTCSPV/T system design is concerned, the key considerations include the following:

- **Optical system:** The parabolic concentrator employed in the hybrid solar system is full spectral reflective mirror. The most cost-effective method is to coat materials such as silver and aluminum on glass or other surface. The spectrally selective interference filter is not so cheap as the primary mirror for its coatings to be difficultly designed and manufactured. Besides, the secondary mirror set upon the focus point could shield sunlight from the solar cell. So it is critical to optimize the structure parameters of the hybrid solar system.
- **Electricity production:** The choices of front glazing, solar cells, as well as packing ratio are important for the final power output.
- **Heat recovery:** Photos below  $E_g$  transmits from the beam filter and then reach the heat receiver. The decisive factors are the choices of absorption coefficient of the tubular receiver, the size of the tube and its displacement. A perfect choice is the evacuated collector tube.

### 2.1. Geometric parameters

Fig. 1 specifies the coordinate system used for describing the parabolic trough solar system. Because the relations between geometric concentration ratio and the apertures and focus lengths of the mirrors are complex, it is necessary to set up a nondimension model to study different size of concentrators and beam filters. Hence the focus length of the concentrator is

chosen as the characteristic length, and the relative apertures of the parabolic concentrator and splitter mirrors are

$$A_c = a_c/f_c, \quad A_s = a_s/f_c \quad (2)$$

The optical axis is along the two focus points, then the incident point on the primary mirror  $P_1$  of the ray  $P_0P_1$  has the coordinates

$$P_1 = \left( X, Y, Z = \frac{X^2}{4} \right) \quad (3)$$

where the focal length is unity in units. Furthermore, the rim angle of the concentrator is

$$\varphi_{\text{rim}} = \arcsin \left( \frac{8A_c}{16 + A_c^2} \right) \quad (4)$$

The incident point  $P_2$  on the beam filter surface has the coordinates

$$P_2 = \left( X, Y, Z = \frac{X^2}{4F_s} + Z_{S0} \right) \quad (5)$$

where  $F_s$  is the relative focus length of the filter,  $F_s = f_s/f_c$ . The two focus points are concurrent, so  $Z_{S0} = 1 - F_s$ . Furthermore, the nondimensional equation of the heat receiver tube is

$$X^2 + (Z - Z_{R0})^2 = \frac{D_R^2}{4} \quad (6)$$

where  $Z_{R0} = 1 - F_s$  and  $D_R$  is the diameter of the receiver tube.

### 2.2. Solar image

The incident rays paralleling to the optical axis are reflected by the primary mirror and the beam filter, then reach the solar cell surface vertically. The size of the solar image on the solar cell plane is determined by the border sunlight of the incident ray cone at every incident point on the concentrator. The equation of

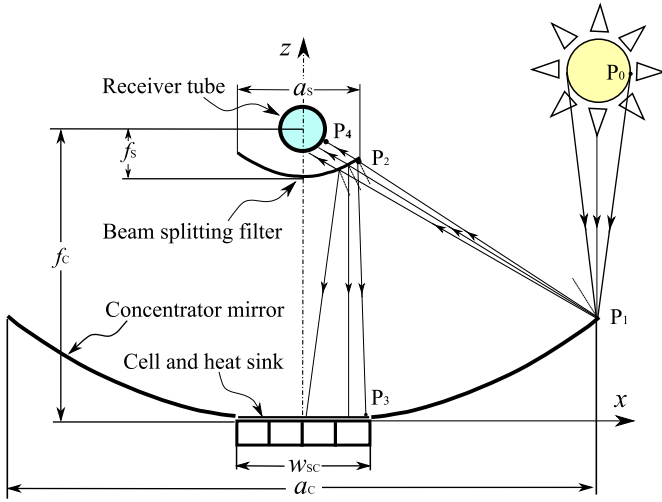


Fig. 1. Schematic diagram of the concentrating beam splitting solar system, shown in two dimensions.

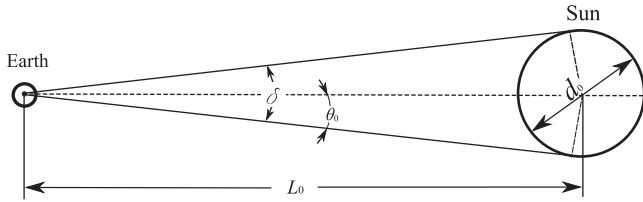


Fig. 2. Solar intercept angle, determined by the distance between the Sun and the Earth.

the border sunlight is as follows:

$$Z = K_1 X - \frac{1}{2} K_1 A_c + \frac{A_c^2}{16} \quad (7)$$

where  $K_1$  is determined by the solar intercept angle  $\delta$ . As shown in Fig. 2, it is evaluated with the following expression:

$$\delta = 2\theta_0 = 2\arctan\left(\frac{d_{\text{Sun}}}{2 \times L_0}\right) \quad (8)$$

where the angle  $\theta_0$  changes from 4.742 mrad in January to 4.584 mrad in July, caused by the Earth elliptical orbit. Taking into account  $d_{\text{Sun}} = 1.392 \times 10^9$  m and  $L_0 = 1.496 \times 10^{11}$  m, then  $\theta_0 \approx 4.65$  mrad and  $|K_1| \approx 215$  is evaluated with Eq. (8).

The position of the border sunlight reaches the cell plane is the function of the structure parameters

$$X_{P_3} = \Gamma_1(K_1; A_c, F_s) \quad (9)$$

The explicit expression of the function  $\Gamma_1$  is explicitly derived according to the Fresnel law in Appendix A. As shown in Fig. 1, the width of the solar image on the cell plane  $W_{sc}$  is evaluated as follows:

$$W_{sc} = w_{sc}/f_c = 2\Gamma_1(K_1; A_c, F_s)|_{K_1 = -215} \quad (10)$$

### 2.3. Heat receiver

Transmitted light through the beam filter is absorbed by the evacuated collector tube set on the focus point of the parabolic collector. As for the non-parallelism of the sunlight, the solar image on the focus plane is not a point but a spot. As shown in

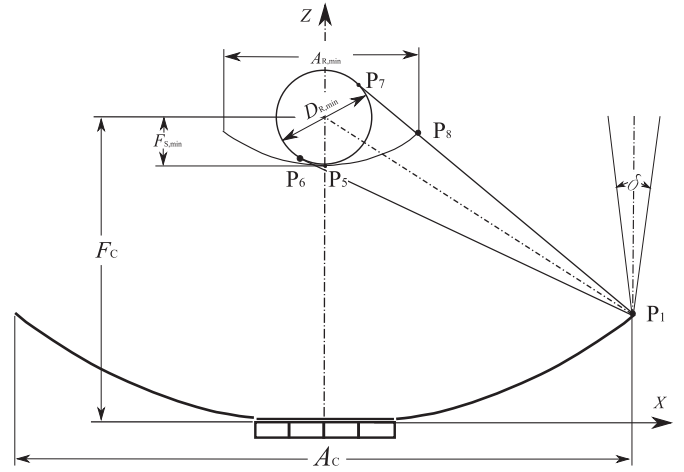


Fig. 3. Diagram of the minimal solar spot on the focal plane with the primary concentration.

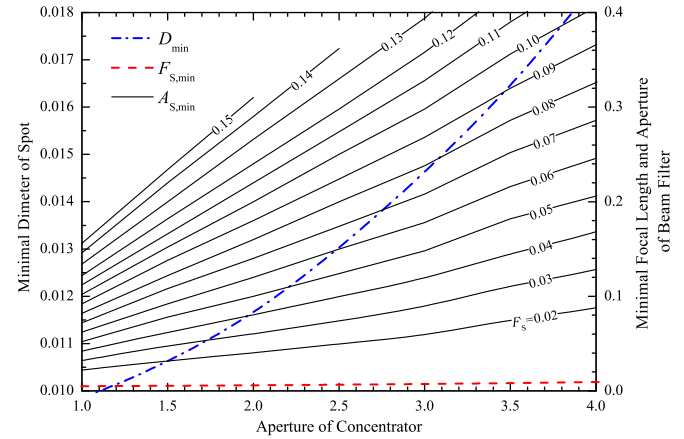


Fig. 4. Minimal solar spot and beam splitting filter at different concentrator apertures.

Fig. 3, the minimal diameter of the spot is given by

$$D_{min} = 2 \left( 1 + \frac{A_c^2}{16} \right) \sin \theta_0 \quad (11)$$

The tube of the heat recovery is obviously larger than the spot,  $D_T > D_{min}$ . In general, it is true that there is energy loss due to the shading of the beam filter, so it needs to use smaller filter to increase the optical efficiency. As shown in Fig. 3, the minimal focus length of the parabolic beam filter is  $F_{s,min} = 0.5D_T$  and generally  $F_s > F_{s,min}$ . The results of  $D_{min}$  and  $F_{s,min}$  are presented in Fig. 4. Furthermore, the minimal aperture is depended on the parameters  $A_c$  and  $F_s$  as the following expression:

$$A_{s,min} = 2X_{P_8} = 2\Gamma_2(K_1; A_c, F_s) \quad (12)$$

The explicit expression of the function  $\Gamma_2$  is explicitly derived in Appendix B and Fig. 4 presents the results with Eq. (12) at different concentrator apertures and different filter focus lengths. It is important to carry out this test criterion  $A_s > A_{s,min}$  in the design work.

### 2.4. Geometric concentration ratio

The geometric concentration ratio is defined as the ratio of effective aperture area  $(A_c - W_{sc})L$  over solar spot area on the cell

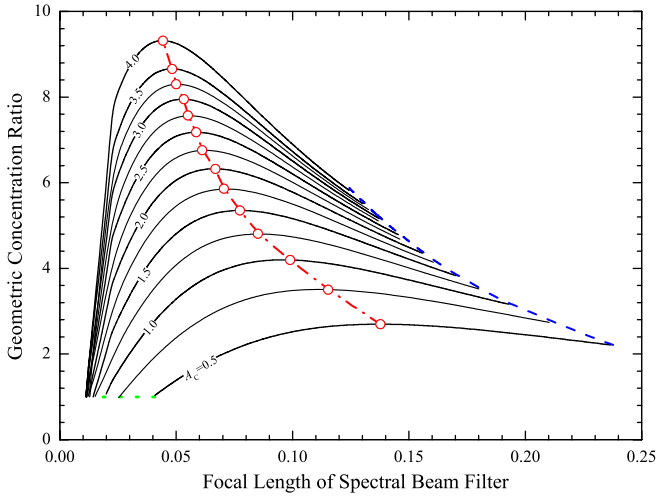


**Fig. 5.** Geometric concentration ratio of the TTCSPV/T system, determined by the concentrator aperture and the focal length of the beam splitting filter.

plane  $W_{SC}L$ ,

$$CR = (A_c - W_{SC}) / W_{SC} \quad (13)$$

As shown in Fig. 5, the evaluation results of geometric concentration ratio with Eq. (13) are presented. As for a size-fixed beam filter, CR increases when the concentrator aperture is enlarged. Because the solar image on the solar cell plane is very large when the focal length of the filter is very small, the lower limit of  $F_s$  is shown as the dot line in the figure. On the other hand, too large  $F_s$  will result in dark spot in the solar image, so its upper limit is evaluated as the dash line in the figure. Furthermore, there is a maximal CR to each  $A_c$  and the optimum design parameters should be selected along the dash dot line in the figure.

### 3. Spatial distribution of irradiance density

The local flux density distribution is very important to the cell because non-uniform illumination produces significant local heating and reduces the efficiency of the cell [14,15].

#### 3.1. Ray trace evaluation

The sun is not a point light source and the three-dimensional model is needed to evaluate the optical characteristics of the TTCSPV/T system. As shown in Fig. 6, the local coordinate system  $X_3Y_3Z_3$ , of which the  $Z_3$ -axis is paralleling to the directed line from local incident point  $P_0$  to the center of the Sun  $O_{SD}$  (it is also parallel to the solar incident vector  $\mathbf{n}_{SD}$ ), is employed to illustrate the incident rays of the solar beam cone. The unit vector of an incident ray  $P_0P_1$  in the beam cone is

$$\mathbf{n}_{X_3Y_3Z_3} = (\sin\beta\cos\alpha, \sin\beta\sin\alpha, \cos\beta)^T \quad (14)$$

The coordinate system  $X_3Y_3Z_3$  can be transformed from the global coordinate system  $XYZ$  by the two parameters  $\gamma$  and  $\theta$  in Fig. 6, so the vector  $\mathbf{n}_{X_3Y_3Z_3}$  in  $XYZ$  coordinate system is obtained by the following equation:

$$\mathbf{n}_{XYZ} = \begin{bmatrix} \cos\gamma\cos\theta & -\sin\theta & \sin\gamma\cos\theta \\ \cos\gamma\sin\theta & \cos\theta & \sin\gamma\sin\theta \\ -\sin\gamma & 0 & \cos\gamma \end{bmatrix} \cdot \mathbf{n}_{X_3Y_3Z_3} \quad (15)$$

where  $\gamma$  is the angle between  $Z_3$ -axis and  $Z$ -axis, and  $\theta$  is the angle made with the positive  $X$ -axis by the projection vector of the  $Z_3$ -axis in the  $XOY$  plane. The parameter equation expression of

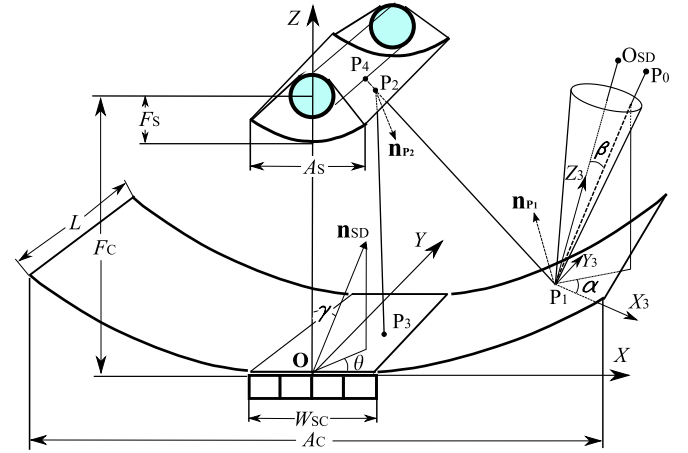


**Fig. 6.** Calculation diagram of the local radiation flux density distribution on the cell and receiver of the concentrating PV/T system.

the incident ray  $P_0P_1$  on the concentrator is

$$\begin{bmatrix} X \\ Y \\ Z \end{bmatrix} = \begin{bmatrix} X_{P_1} \\ Y_{P_1} \\ Z_{P_1} \end{bmatrix} + \begin{bmatrix} n_1 \\ n_2 \\ n_3 \end{bmatrix} \cdot t \quad (16)$$

where  $n_1, n_2$  and  $n_3$  are the component of the vector  $\mathbf{n}_{XYZ}$ . The unit normal vector at  $P_1$  is given with Eq. (A.1). The equation of the reflection ray  $P_1P_2$ , derived from Eqs. (16) and (A.1) according to Fresnel reflection law, is

$$\begin{bmatrix} X \\ Y \\ Z \end{bmatrix} = \begin{bmatrix} X_{P_1} \\ Y_{P_1} \\ Z_{P_1} \end{bmatrix} + \begin{bmatrix} n_4 \\ n_5 \\ n_6 \end{bmatrix} \cdot t \quad (17)$$

where  $n_4, n_5$  and  $n_6$ , the component of the unit normal vector  $\mathbf{n}_{P_1P_2}$  of the ray  $P_1P_2$ , can be expressed as the following equation:

$$\begin{bmatrix} n_4 \\ n_5 \\ n_6 \end{bmatrix} = \frac{1}{X_{P_1}^2 + 4} \begin{bmatrix} (X_{P_1}^2 - 4)n_1 - 4X_{P_1}n_3 \\ -n_2(X_{P_1}^2 + 4) \\ (4 - X_{P_1}^2)n_3 - 4X_{P_1}n_1 \end{bmatrix} \quad (18)$$

Using Eqs. (5) and (A.2), the position of the incident point on the beam filter surface can be estimated. Furthermore, the unit normal vector  $\mathbf{n}_{P_2}$  at  $P_2$  is calculated with Eq. (A.4) and the equation of its reflection ray  $P_2P_3$  can be obtained by

$$\begin{bmatrix} X \\ Y \\ Z \end{bmatrix} = \begin{bmatrix} X_{P_2} \\ Y_{P_2} \\ Z_{P_2} \end{bmatrix} + \begin{bmatrix} n_7 \\ n_8 \\ n_9 \end{bmatrix} \cdot t \quad (19)$$

where  $n_7, n_8$  and  $n_9$ , the component of the unit normal vector  $\mathbf{n}_{P_2P_3}$  of the ray  $P_2P_3$ , can be expressed as the following equation:

$$\begin{bmatrix} n_7 \\ n_8 \\ n_9 \end{bmatrix} = \frac{1}{X_{P_2}^2 + 4F_s^2} \begin{bmatrix} (X_{P_2}^2 - 4F_s^2)n_4 - 4X_{P_2}n_6 \\ -n_2(X_{P_2}^2 + 4F_s^2) \\ (4F_s^2 - X_{P_2}^2)n_6 - 4F_sX_{P_2}n_4 \end{bmatrix} \quad (20)$$

Finally the incident point  $P_3$  at the cell is obtained using Eq. (19), and the masses of this point make up the solar image on the cell. On the other hand, the transmitted part of the ray  $P_1P_2$  through the filter hits on the receiver tube surface at the point  $P_4$ . Very short as the optical path length in the filter body is, the displacement offset of the light ray can be ignored and the position of  $P_4$  is given by Eqs. (6) and (19).

### 3.2. Sampling points on the solar disk

Each incident ray in the beam corn has one source point (the solid point as shown in Fig. 7)  $P_0$  on the solar disk. The grid number of the solar disk is  $I_{SD}^2$  (let  $I_{SD}$  be equal to  $J_{SD}$ ) while the number of points used for calculation is less, and it is approximately as

$$N_{SD} = \lim_{I_{SD} \rightarrow \infty} \frac{\pi}{4} I_{SD}^2 \quad (21)$$

As shown in Figs. 6 and 7, the coordinate system  $X_{SD}O_{SD}Y_{SD}$  on the solar disk can be translated from the  $X_3O_3Y_3$  along the  $Z_3$  positive axis. The direction of the incident rays is determined by the incident angles  $\alpha$  and  $\beta$  with the sampling points in Fig. 7:

$$\alpha = \begin{cases} 2\pi - \arccos\left(\frac{2i - I_{SD}}{\sqrt{I_{SD}^2 + J_{SD}^2}}\right) & \text{for } j \leq \frac{J_{SD}}{2} \\ \arccos\left(\frac{2i - I_{SD}}{\sqrt{I_{SD}^2 + J_{SD}^2}}\right) & \text{for } j > \frac{J_{SD}}{2} \end{cases} \quad (22)$$

$$\beta = \arctan\left(\sqrt{\frac{(2i - I_{SD})^2 + (2j - J_{SD})^2}{I_{SD}^2 + J_{SD}^2}} \tan\theta_0\right) \quad (23)$$

### 3.3. Effect of sunshape

The numerical method is to use finite rays instead of infinite sunlight rays to simulate the actual optical characteristics. The distribution of the sampling points in the concentrator is uniform and its total number is  $N_C \times N_C$ , so the total number of the incident ray  $N_{tot}$  is  $N_C^2 N_{SD}$ . These rays indicate the total solar energy collected by the concentrator of the TTCSPV/T system and the energy for each ray is

$$e_0 = \frac{E_0(A_C - W_{SC})L}{N_{tot}} \quad (24)$$

where  $E_0$  is the direct solar irradiance in  $W/m^2$  on a plane perpendicular to the incident sun rays.

The solar cell and heat receiver are then divided into many small elements to evaluate the irradiation density distribution, and for the cell and receiver elements it can be obtained by the

following expression, respectively:

$$E_{ij,SC} = \frac{\sum_{k=1}^{N_{ij}} e_{k,SC}}{\Delta_{ij,SC}} = \frac{N_{ij} e_0 \rho_C \rho_S}{\Delta_{ij,SC}} \quad (25)$$

$$E_{ij,R} = \frac{\sum_{k=1}^{N_{ij}} e_{k,R}}{\Delta_{ij,R}} = \frac{N_{ij} e_0 \rho_C (1 - \rho_S)}{\Delta_{ij,R}} \quad (26)$$

where  $ij$  is the grid mark number,  $N_{ij}$  is the number of rays included in the grid,  $\Delta_{ij}$  is the area of the grid,  $e_k$  is the energy of the  $k$ th ray, the concentrator reflectivity  $\rho_C$  is 0.9, and the reflectivity of the beam filter with the performance in Eq. (1)  $\rho_S$  is equal to 0.77 according to the proposed solar spectral irradiance by Gueymard et al. [16]. Furthermore, the relative irradiance density  $\xi$  is defined as the ratio of the local irradiance density over  $E_0$ , so Eqs. (25) and (26) become

$$\xi_{ij,SC} = \frac{\sum_{k=1}^{N_{ij}} \xi_{k,SC}}{\Delta_{ij,SC}} = \frac{N_{ij}(A_C - W_{SC})L\rho_C\rho_S}{\Delta_{ij,SC}N_{tot}} \quad (27)$$

$$\xi_{ij,R} = \frac{\sum_{k=1}^{N_{ij}} \xi_{k,R}}{\Delta_{ij,R}} = \frac{N_{ij}(A_C - W_{SC})L\rho_C(1 - \rho_S)}{\Delta_{ij,R}N_{tot}} \quad (28)$$

It is not the truth that each ray is coequal due to the solar brightness distribution that we called sunshape. Limb darkening and atmospheric attenuation are responsible for the radiant intensity distribution of the solar disk. Furthermore, the extra-terrestrial solar disk has a limb darkening caused by the inner radial temperature profile within the Sun. The circumsolar ratio (CSR) is a simple concept to describe the features of the sunshape, and the CSR ( $\chi$ ) is defined as the integrated intensity over the solar disk  $E_{CS}$ , divided by the integrated intensity of the circumsolar region  $E_{Sun}$ :

$$\chi = \frac{E_{CS}}{E_{Sun}} \quad (29)$$

The first sunshape model, often referred as the Kuiper distribution [17], describes the limb darkening from the disk center out to 4.65 mrad. It was created from solar observations made prior to 1953 and sometimes used in modeling of the solar concentrating systems. Recently however, after the publication of new sunshapes obtained by the Lawrence Berkeley Laboratories (LBL) and the German Aerospace Center (DLR), the typical average solar brightness profiles with a CSR of about 0%, 5%, 10%, 20%, 30%, and 40% were generated by Neumann et al. [18]. Using the vast database of LBL and DLR, Buie et al. [19] proposed a sunshape model that is independent of geographic location and described an algorithm, which can be used to model different sunshapes for simulating solar concentrating systems,

$$\phi(\beta) = \begin{cases} \frac{\cos(0.326\beta)}{\cos(0.308\beta)} & \text{for } \beta \leq 4.65 \text{ mrad} \\ e^{\kappa\beta^\mu} & \text{for } \beta > 4.65 \text{ mrad} \end{cases} \quad (30)$$

where  $\beta$ , the radial angular displacement, is calculated with Eq. (23),  $\kappa$  and  $\mu$  are

$$\kappa = 0.9 \ln(13.5\chi) \chi^{-0.3}$$

$$\mu = 2.2 \ln(0.52\chi) \chi^{0.43} - 0.1$$

The names of the six typical profiles (CSR 0, CSR 5, CSR 10, CSR 20, CSR 30, and CSR 40) do not exactly correspond to the CSR of each profile used for simulation. For example, the 0% and 5% profiles have the CSR of 2.7% and 5.01%, respectively [18]. As shown in Fig. 8, the evaluation results of sunshape using Buie model illustrate the adequacy of precision of Eq. (30). Besides the six typical profiles, the single mean DLR profile, generated by averaging the profiles CSR 0 to CSR 40 using the statistical frequency of occurrence of each profile, is also presented in Fig. 8.

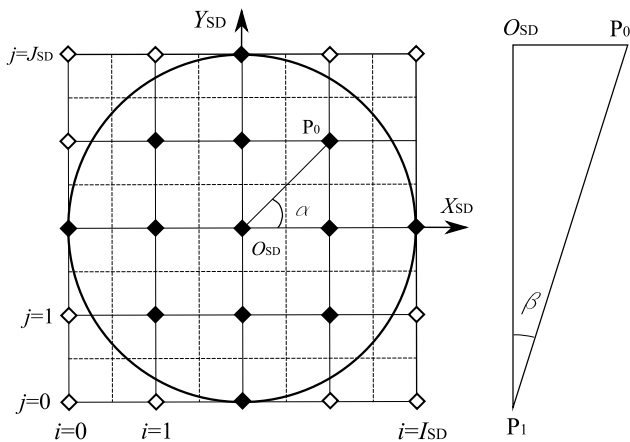


Fig. 7. Schematic diagram of the solar disk grid meshing. The solar intensity profile is radial symmetry, so the meshing elements of the solar disk are uniform and  $I_{SD} = J_{SD}$ .



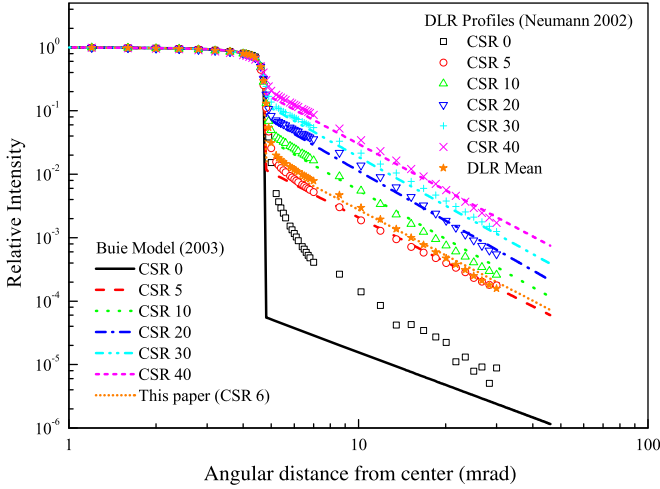


Fig. 8. Observed data collated by [18] and sunshapes generated with Eq. (30).

Neumann et al. [18] suggested using this single sunshape profile for annual analysis of concentrating optics performance. And it has the CSR of 6.3% in the Buie model (named CSR 6 as shown in Fig. 8). So CSR 6 is employed in the present analysis to provide an approximation to the DLR mean profile. Hence, considering the radial brightness distribution of the sun, the local relative irradiance density with Eqs. (27) and (28) can be rewritten as

$$\zeta_{ij,SC} = \frac{(A_c - W_{SC})L\rho_c\rho_s}{\Delta_{ij,SC}N_{tot}} \sum_{k=1}^{N_{ij}} \zeta\phi(\beta)_{k,SC} |_{\chi=6.3\%} \quad (31)$$

$$\zeta_{ij,R} = \frac{(A_c - W_{SC})L\rho_c(1-\rho_s)}{\Delta_{ij,R}N_{tot}} \sum_{k=1}^{N_{ij}} \zeta\phi(\beta)_{k,R} |_{\chi=6.3\%} \quad (32)$$

where the coefficient  $\zeta$  is a constant given by the following normalized distribution:

$$2\pi \int_0^{\beta_{max}} \zeta\phi(\beta)\sin(\beta) d\beta = 1$$

### 3.4. Effect of grid number

The accuracy of the ray trace method is dependent upon the grid number of concentrator and solar disk. Based on the preceding calculation procedure, the computer code in FORTRAN language is written. The larger the number of sampling points on the concentrator is, the more true the evaluation results become on the solar cell. While the true value can only be obtained exactly by tracing an infinite number of energy bundles in the numerical experiment, so the “true” value is chosen corresponding to very large grid number (250 000 elements on concentrator and 31 417 ones on solar disk). The accuracy of different meshing conditions is evaluated by using the standard deviation with the “true” value,

$$\sigma = \left[ \frac{1}{N_{SC}} \sum_{k=1}^{N_{SC}} (\zeta_k - \zeta_{k,true})^2 \right]^{1/2} \quad (33)$$

The numerical experiments are carried out with the AMD Athlon(tm) 64 Processor 3000+, and the parameters are listed in Table 1. Fig. 9 shows the convergence of the irradiation density in the solar cell plane with the number of grid. It is clear that the standard deviation goes essentially to zero as the number of elements increases. On the other hand, high accuracy results mean an increase in the number of rays and more processing time. It is significant to strike the balance between solution, which is the sufficiently accurate for the requirements of the problem,

and the consumption of CPU time. It is proposed that  $N_c = 100$  and  $I_{SD} = 150$  in the following evaluation proceeding, so the standard deviation is less than 0.05, and the evaluation time is about 513 s. The evaluation results are shown in Figs. 10–12.

The local irradiance density on the spectral beam filter surface shown in Fig. 10 is very uniform except for the narrow small central part due to the shielding of the beam filter. As shown in Fig. 11,

Table 1  
Evaluation parameters of TTCSPV/T system.

Parameters	Value
Geometric concentration ratio	7.0
Aperture of the concentrator	2.4
Aperture of the beam filter	0.2
Relative focal length of the beam filter	0.06
Diameter of the heat receiver tube	0.056
Length of the trough	1.0
Characteristic length	420 mm
Grid number of the evaluation surfaces	100 × 100

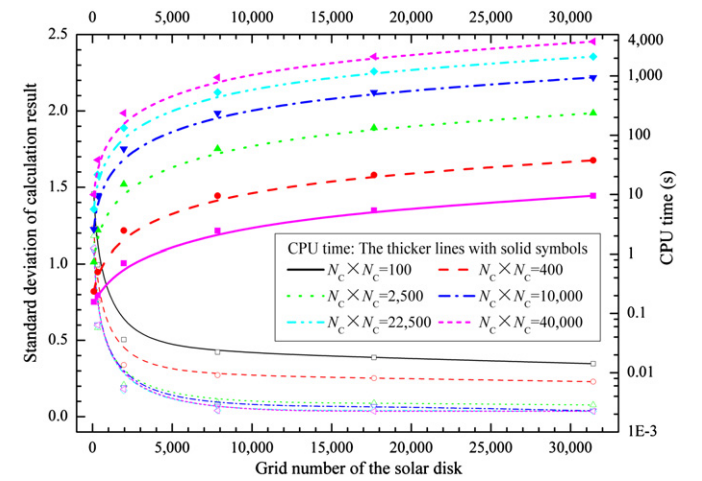


Fig. 9. Standard deviation of the evaluation results and the CPU time consumed at different number of elements.

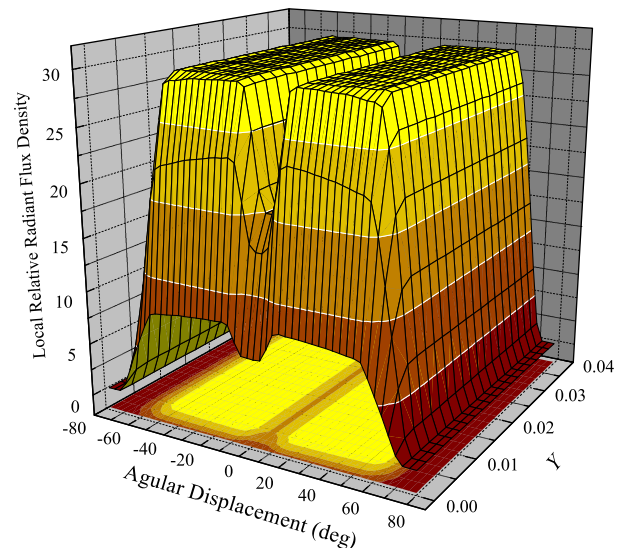


Fig. 10. Local incident radiation flux density distribution on the beam splitting filter. The relative focal length of the filter is 0.06,  $A_c = 2.4$ ,  $D_R = 0.056$ ,  $L = 1.0$ ,  $CR = 7.0$ ,  $N_c = 100$  and  $I_{SD} = 150$ .

the relative irradiance density on the central part of the solar cell is higher than two sides, and the maximal local radiance density is about 6. The radiation flux density distribution on the heat receiver surface is presented in Fig. 12, and it is minimal in bottom center of the tube. It is clear that the distribution is homogeneous in the direction along the trough except for the very short parts of both ends. So the radiation density distribution on the cross-section of the trough is discussed in the following section.

The size of the receiver tube is limited within  $D_{\min}$  by Eq. (11) and  $F_s$ . The radiation flux distribution on the cross-section of the receiver at different diameters is shown in Fig. 13, and it increases at smaller tube. Though little loss occurs on the rim part, it is beneficial for the choosing suitable spot receiver tubes at lower cost.

### 3.5. Effect of alignment error

In the previous discussion, the focuses of the two parabolic mirrors and the center of the tube are coincident points, while it

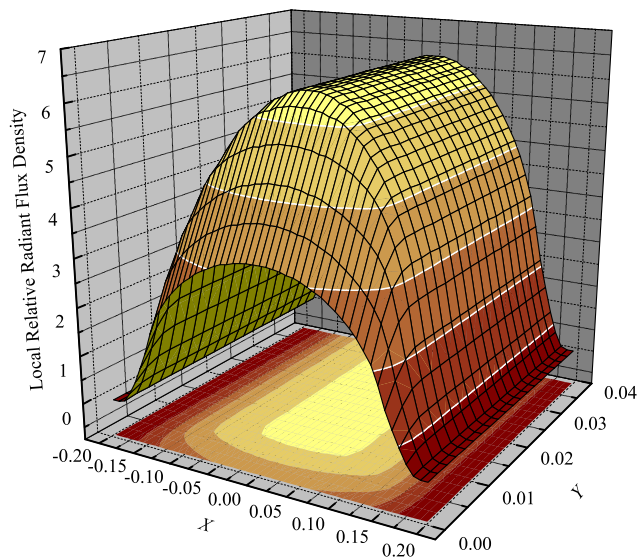


Fig. 11. Local incident radiation flux density distribution on the solar cells, the same evaluation parameters listed in Fig. 10.

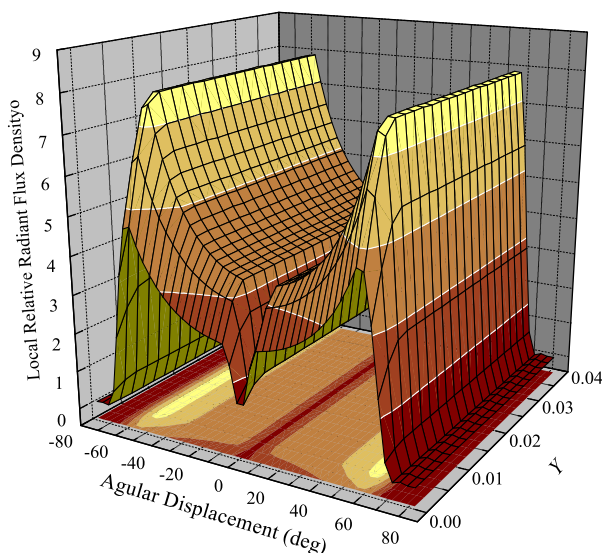


Fig. 12. Local incident radiation flux density distribution on the heat receiver tube, the same evaluation parameters listed in Fig. 10.

cannot be the truth in actual experiments. It is necessary to consider the effect of the alignment error, so the position of the base points in Eqs. (5) and (6) is

$$Z_{S0} = 1 - F_s + \Delta Z_{S0}, \quad Z_{R0} = 1 - F_s + \Delta Z_{R0} \quad (34)$$

Figs. 14 and 15 show the various flux density distributions on the beam filter and solar cell, respectively. Furthermore, the distribution on the tube does not change and it is the same as that in Fig. 12. The spot on the filter surface becomes narrow as the alignment error on Z-axis increases from negative error to positive error; meanwhile, the uniformity of the radiant flux density becomes worse considering the effect of the alignment error. Noticeable changes take place in the flux distribution on the cell because of the two-stage concentrating system. It can be seen from the figure that smaller positive alignment error is allowed in actual experiment.

The variation of the flux density distribution on the tube is shown in Fig. 16, while the distributions on the filter and solar cell do not change. The area of the spot on the tube decreases as the alignment error on Z-axis increases. Moreover, the radiant flux density becomes more uniform at plus alignment error, and thus

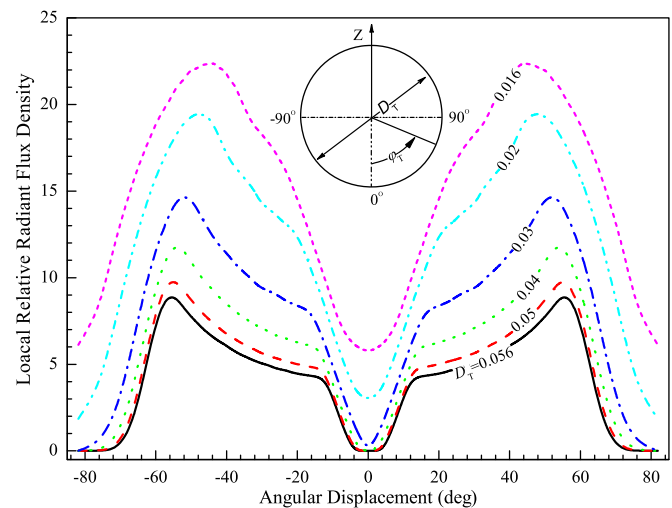


Fig. 13. Local incident radiation flux density distribution on the heat receiver tube with the relative diameter of the tube  $0.016 \leq D_R \leq 0.056$ .

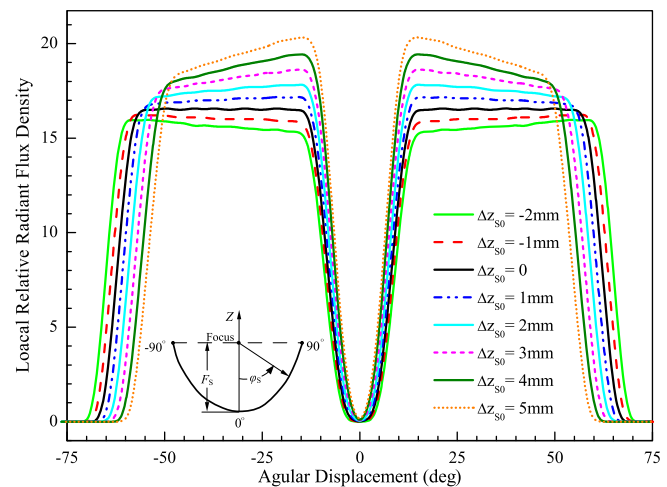
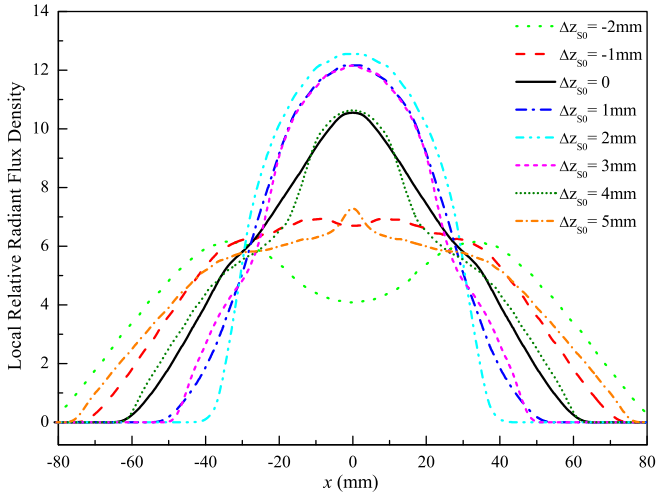
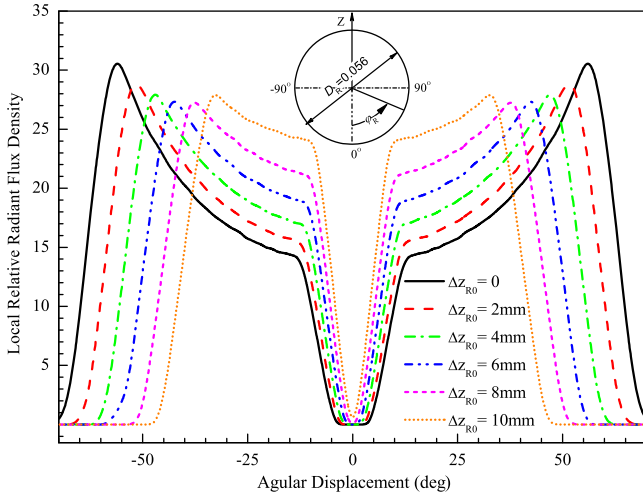


Fig. 14. Local incident radiation flux density distribution on the beam splitting filter. The focal length of the concentrator is 420 mm, and the alignment error on z-axis of the beam splitting filter is  $-2 \text{ mm} \leq \Delta z_{S0} \leq 5 \text{ mm}$ .



**Fig. 15.** Local incident radiation flux density distribution on the solar cell. The focal length of the concentrator is 420 mm, and the alignment error on z-axis of the beam splitting filter is  $0 \text{ mm} \leq \Delta z_{s0} \leq 10 \text{ mm}$ .



**Fig. 16.** Local incident radiation flux density distribution on the heat receiver tube. The focal length of the concentrator is 420 mm, and the alignment error on z-axis of the receiver tube is  $0 \text{ mm} \leq \Delta z_{r0} \leq 10 \text{ mm}$ .

homogeneous radiation distribution is suitable for absorption of the receiver.

### 3.6. Effect of tracking error

Tracking structure is needed for the concentrators working with concentration ratio of over 5, especially for the two-stage concentrating system [2]. The parabolic concentrators of the TTCSPV/T are mounted on a two-axis tracking unit to keep the sun rays focused on the solar cells and the receiver tubes throughout the day, and in this situation the declination-right ascension tracking structure is adopted. So there are two tracking angle variables corresponding to the two tracking directions, one of which is the declination angle  $\gamma_{De}$  and is approximately given by the expression [20]

$$\gamma_{De} = 23.45 \sin \left( 2\pi \frac{N_{Day} + 284}{365} \right) \quad (35)$$

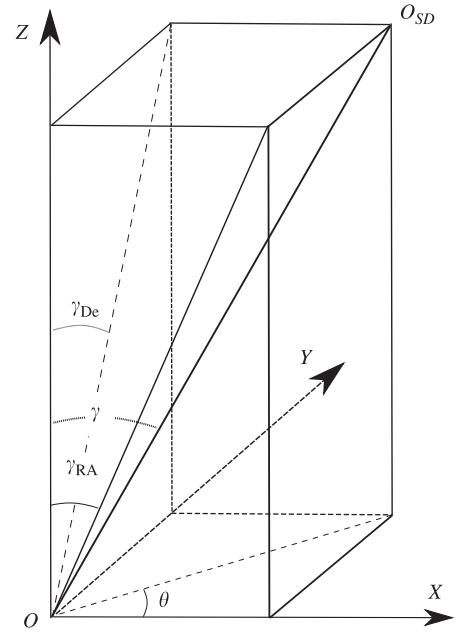


**Fig. 17.** Relationship between tracking angles ( $\gamma_{De}$  and  $\gamma_{RA}$ ) of the two-axis tracking unit and parameters ( $\gamma$  and  $\theta$ ) in the mathematical model.

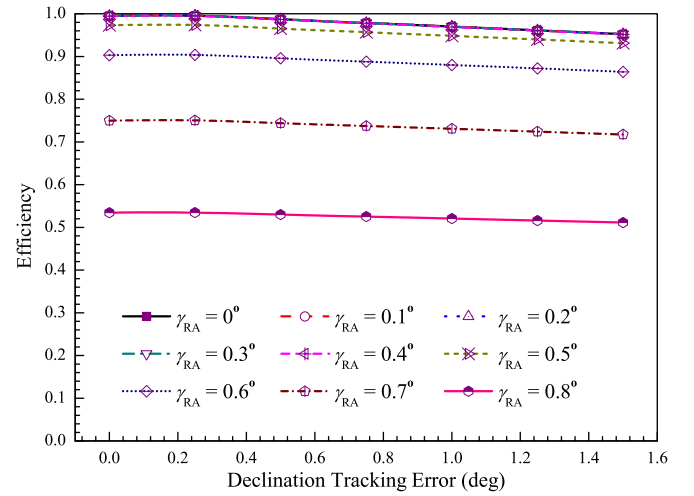


**Fig. 18.** Effect of the tracking errors in the declination-right ascension tracking structure.

where  $N_{Day}$  is the day of the year. The other is the right ascension angle  $\gamma_{RA}$  and it changes at the constant speed of  $15^\circ$  per hour. The tracking results of the unit can be simulated by the two angles. Unfortunately the two variables are not the tracking parameters ( $\gamma$  and  $\theta$ ) described in the mathematical model in Fig. 6, and the relationship is given in Fig. 17 by the expression

$$\gamma = \arctan \sqrt{\tan^2 \gamma_{De} + \tan^2 \gamma_{RA}}, \quad \theta = \arcsin \frac{\tan \gamma_{De}}{\sqrt{\tan^2 \gamma_{De} + \tan^2 \gamma_{RA}}} \quad (36)$$

The optical efficiency of the tracking unit in different tracking errors is shown in Fig. 18. It decreases slightly as the declination tracking error increases while it drops badly as the tracking error in the right ascension axis larger than  $0.6^\circ$ . So the precision reducer with the output speed of  $15^\circ$  per hour is needed in right



ascension axis tracking, while a hand-operating mechanism can meet the requirement of the declination axis tracking.

### 3.7. Optimal design

In the previous discussion the geometric concentration ratio (including the maximum ratio) is given in Fig. 5. However, it is just an average irradiance density on the surface of the optical elements, and the detailed solar irradiation distribution on the cell is very inhomogeneous. Furthermore, it will lead to temperature rising and the reduction of the output [3,14].

In general the collection area is definite and the design task is to find out the optimal focal length of the beam filter. Figs. 19 and 20 show the evaluation results at different beam filter parameters, while the aperture of the concentrator is 2.4 and the concentration ratio is obtained from Fig. 5. Considering the heat sink of the solar cell and cell area to be employed, the focal length  $F_s=0.3$  is an option for natural cooling while a larger focal length ( $F_s=0.8$ ) is better for active cooling.

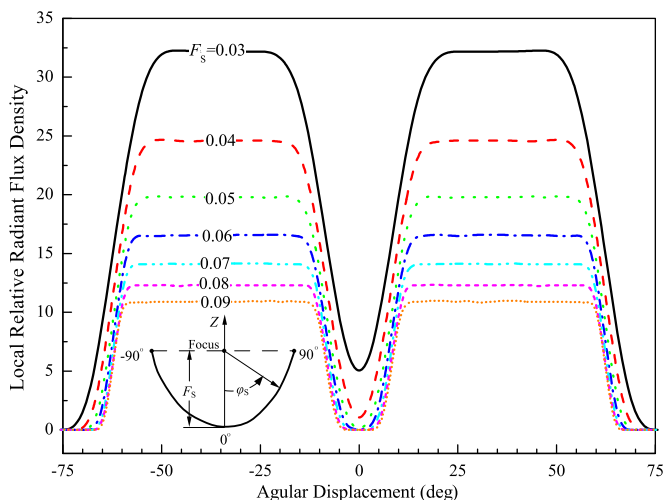


**Fig. 19.** Local incident radiation flux density distribution on the beam splitting filter at different focal lengths. The relative focal length is  $0.3 \leq F_s \leq 0.9$ , and  $A_c=2.4$ ,  $D_R=0.056$  and  $L=1.0$ .

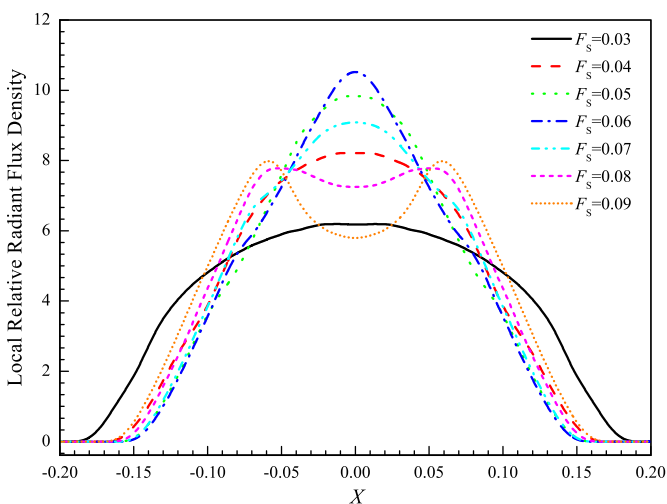


**Fig. 20.** Local incident radiation flux density distribution on the solar cells at different beam filters. The evaluation parameters are the same with those listed in Fig. 19.

## 4. Spectral characteristic of irradiation flux

The solar cell is a spectrally selective device and its properties are extremely dependent upon the spectral characteristic of the incident radiation flux. So it is critical to analyze the spectral properties of the elements (concentrator, beam splitting filter and the cell) of the system.

The surface of the concentrating mirror is full spectral reflective and aluminum with protective coating is generally used [9]. The spectral reflectivity of the concentrator surface tested with the U-4100 spectrophotometer of HITACHI Company is shown in Fig. 21, hence the total reflectivity is about 0.88. The total reflectivity of the solar cell is  $\rho_{SC}=0.04$  with the anti-reflection coating, and its electrical property is demonstrated by the quantum efficiency shown in Fig. 21.

### 4.1. Spectral beam splitting filter

The beam filter is the key element in the concentrating beam splitting system [6]. The surface is needed to be deposited a wide spectrally selective coating. Imenes et al. [21] proposed a broad-band wide-angle interference filter for the tower concentrating system, and the filter results in a bandpass region of spectral width  $\Delta\lambda \approx 500$  nm (from 590 to 1082 nm). However, it is not suitable for the splitting filter used in TSCPV system whose concept is described in Eq. (1), so special design is to be made.

A powerful coating design technology, needle optimization method, has been developed [22,23]. As to beam splitting filters, the nonabsorbing dielectric coating is a good choice. One pair of materials with  $n_L=1.471$ ,  $n_H=2.314$  is employed for the optimization. The design targets for this problem are as follow:  $\rho=1$  in the spectral range from 380 to 1100 nm, and  $\rho=0$  for the spectral range from 1100 to 2500 nm. The final design of the complex multilayered film stack is specified by the formulas below.

A 0.2128H 0.7902L 0.4193H 0.4097L 0.3687H 0.6067L 0.3832H  
0.5770L 0.4246H 0.8421L 0.5170H 0.7458L 0.4857H 0.8350L  
0.5289H 0.8247L 0.5538H 0.9101L 0.6675H 1.1758L 0.6771H  
0.9025L 0.6184H 0.9516L 0.7260H 1.2430L 0.7026H 1.2898L  
0.8379H 1.2329L 0.8180H 1.4306L 0.9238H 1.4341L 0.8843H  
1.4443L 0.8562H 1.4450L S.

In the formulas, A stands for air (ambient medium), S stands for the substrate with a refractive index of 1.518, and H and L are

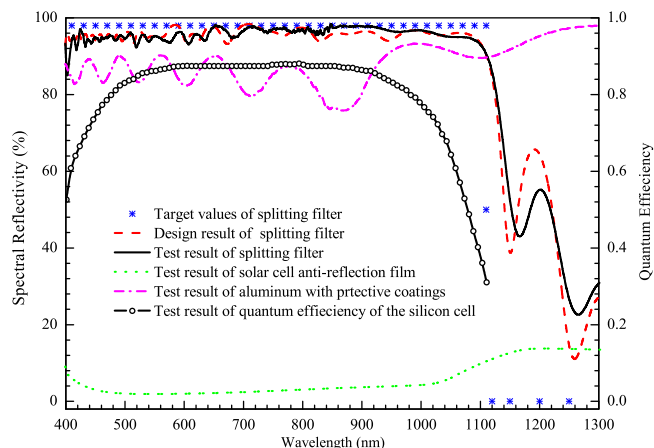


**Fig. 21.** Spectral properties of the optical elements: the spectral reflectivity of the concentrator mirror, the beam splitting filter and solar cell anti-reflection film; the quantum efficiency of the silicon solar cell.

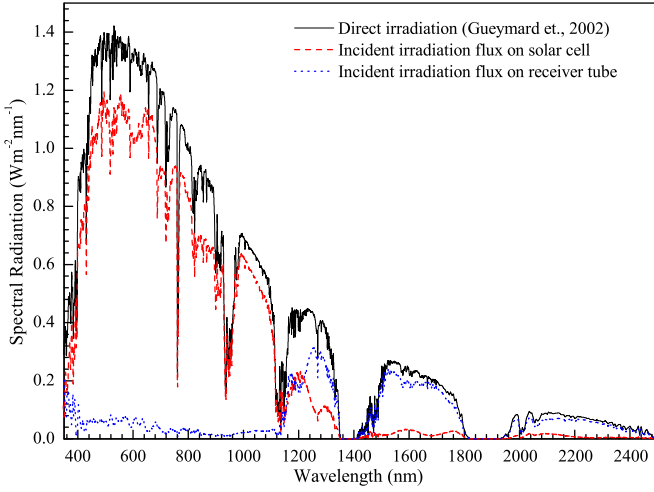


Fig. 22. Spectral distribution of the solar irradiation flux on the solar cell surface and heat receiver surface.

the symbols of the high and low refractive index materials,  $\text{Nb}_2\text{O}_5$  and  $\text{SiO}_2$ , respectively. Coating is carried out on the RAS-1100C magnetron sputtering plant made by Shincron Co. Ltd. Fig. 21 shows the test results of reflectivity. It is clear that the average residual reflectance of the splitting filter coating between the test results and the design curve is less than 0.02.

#### 4.2. Spectral distribution of irradiation flux

Gueymard et al. [16] proposed a representative solar spectral irradiance for the terrestrial application, including the direct radiation for the concentrating system in Fig. 22. The incident solar direct radiation on the concentrator surface is given by the equation

$$E_0 = \int_0^\infty E_{0,\lambda} d\lambda \quad (37)$$

where  $E_0$  is the spectral radiation flux density. And the spectral distributions of the radiation on the solar cell and heat receiver are obtained by the following expressions, respectively:

$$E_{SC} = \int_0^\infty E_{SC,\lambda} d\lambda = \int_0^\infty (1 - \rho_{SC,\lambda}) \rho_{S,\lambda} \rho_{C,\lambda} E_{0,\lambda} d\lambda \quad (38)$$

$$E_R = \int_0^\infty E_{SC,\lambda} d\lambda = \int_0^\infty (1 - \rho_{R,\lambda}) T_{S,\lambda} \rho_{C,\lambda} E_{0,\lambda} d\lambda \quad (39)$$

where  $\rho_{C,\lambda}$  and  $\rho_{S,\lambda}$  are the spectral reflectivity of the mirrors, and  $T_{S,\lambda}$  is the transmissivity of the splitting filter and is given by  $T_{S,\lambda} = 1 - \rho_{S,\lambda}$ . To describe the utilization efficiency of the solar energy, the overall optical efficiency of the system is defined as

$$\eta_0 = \frac{E_{SC} + E_R}{E_0} \quad (40)$$

Using the optical properties of the elements shown in Fig. 21, the spectral distribution of the radiation flux density is evaluated with Eqs. (38) and (39) in Fig. 22. It is clear that using the beam splitting technology the heat load can be reduced by 20.7% of the overall incident radiation energy on the solar cell. And the figure shows that about 10.5% of the total solar energy can be recovered by the receiver. Furthermore, the overall optical efficiency is 0.764 in the condition of standard AM1.5 solar irradiation with Eq. (40).

## 5. Conclusions

A concentrating PV/T hybrid solar system using beam splitting technology is proposed. The solar cell components are placed

below the aperture plane of the concentrator and this is helpful for improving the heat transfer of the sink to the environment. Furthermore, the evacuated collector tube is employed in the trough system to recover the invalid radiation for photovoltaic conversion, and heat energy of moderate temperature (about 250–300 °C) can be obtained. The two axis declination-right ascension tracking unit of TTCSPV/T system is driven by a decelerator with nominal power 10 W.

The detailed optical model has been conducted to predict the optical properties of the hybrid solar system. It is nondimensional and using the focal length of the concentrator as the characteristic length. The model has been divided into three sections for different purpose. The first section is the two-dimensional geometric analysis model, which is used to evaluate the geometry concentration ratio and the size of the solar image at different concentrator aperture together with the focal length of the filter. The result is shown in Fig. 5 and it is critical to choose proper parameters. The second part is the three-dimensional optical model and ray tracing method is used to evaluate the spacial distribution of the irradiation flux on the elements. The model involves the effect of the solar brightness distribution, the alignment error on the optical axis and the tracking error. Furthermore, optimization of the structure parameters is studied, and the focal length of the beam filter extremely affects the radiation distribution on the cell. The last one is the analysis model for the spectral distribution on the elements of the TTCSPV/T system shown in Fig. 22. The special beam splitting filter is designed with needle optimization method and is manufactured using magnetron sputtering technology. The results show that the heat load of the cell can be reduced by 20.7%, and 10.5% of the total incident solar energy can be recovery by the receiver. The overall optical efficiency in theory is up to 0.764 with the optimized splitting coating.

## Acknowledgements

The work is supported by the National Natural Science Foundation of China (nos. 50576092 and 50736005). The authors also thank the help of Prof. Wang H.Q.

## Appendix A. Incident point on the solar cell

The unit vector of the normal line at the incident point  $P_1$  of the parabolic collector in Fig. 1 is

$$\mathbf{n}_{P_1} = \frac{1}{\sqrt{X_{P_1}^2 + 4}} (-X_{P_1}, 0, 2) \quad (A.1)$$

According the Fresnel law, the equation of the reflection ray at point  $P_1$  is

$$Z = K_2 X + B_2 \quad (A.2)$$

where  $K_2 = (-K_1 A_C^2 - 8A_C + 16K_1)/(A_C^2 - 8K_1 A_C - 16)$  and  $B_2 = A_C^2/16 - \frac{1}{2} K_2 A_C$ . With Eqs. (5) and (A.2) the incident point  $P_2$  on the beam filter is

$$X_{P_2} = 2F_S K_2 + 2\sqrt{F_S^2 K_2^2 + F_S(B_2 - Z_{S0})} \quad (A.3)$$

As is the same with the collector, the unit vector of the normal line at the incident point  $P_2$  of the beam filter in Fig. 1 is

$$\mathbf{n}_{P_2} = \frac{1}{\sqrt{X_{P_2}^2 + 4F_S^2}} (X_{P_2}, 0, -2F_S) \quad (A.4)$$

So the equation of the reflection ray at point  $P_2$  is

$$Z = K_3 X + B_3 \quad (A.5)$$

where  $K_3 = -(K_2 X_{p_2}^2 + 4F_S X_{p_2} - 4K_2 F_S) / (X_{p_2}^2 - 4K_2 F_S X_{p_2} - 4F_S^2)$  and  $B_2 = X_{p_2}^2 / 4F_S - K_3 X_{p_2}$ . With Eq. (A.5) the image spot on the solar cell plane for the border incident light is as follows:

$$X_{p_3} = \frac{F_S A_1^4 + (2F_S + 1)A_1 - 2K_2 A_1 + F_S - 1}{K_2 A_1^2 + 2A_1 - K_2} \quad (\text{A.6})$$

where  $A_1$  is just an expression to simplify Eq. (A.6) and it is

$$A_1 = K_2 + \sqrt{K_2^2 + 1 - \frac{1}{F_S} - \frac{K_2 A_C}{2F_S} + \frac{A_C}{16F_S}} \quad (\text{A.7})$$

## Appendix B. Minimal aperture of the beam filter

The boundary point of the beam filter  $P_8$  shown in Fig. 3 is on the border ray of the concentrator primary reflection, and its incident sunlight has  $K_1 = -215$ . According to Eqs. (5) and (A.3), the explicit expression of  $\Gamma_2$  is

$$X_{p_8} = \frac{(860F_S + A_2)A_C^2 - 32F_S A_C + (16A_2 - 13760F_S)}{2(A_C^2 - 1720A_C - 16)} \quad (\text{B.1})$$

where  $A_2$  is defined as follows:

$$A_2 = \sqrt{F_S(A_C^2 + 1720A_C + 739616F_S - 16)} \quad (\text{B.2})$$

## References

- [1] R.M. Swanson, The promise of concentrators, *Progress in Photovoltaics* 8 (1) (2000) 93–111.
- [2] A. Luque, G. Sala, I. Luque-Heredia, Photovoltaic concentration at the onset of its commercial deployment, *Progress in Photovoltaics* 14 (5) (2006) 413–428.
- [3] E. Radziemska, The effect of temperature on the power drop in crystalline silicon solar cells, *Renewable Energy* 28 (1) (2003) 1–12.
- [4] A. Royne, C.J. Dey, D.R. Mills, Cooling of photovoltaic cells under concentrated illumination: a critical review, *Solar Energy Materials and Solar Cells* 86 (4) (2005) 451–483.
- [5] W. Blocker, High-efficiency solar energy conversion through flux concentration and spectrum splitting, *Proceedings of the IEEE* 66 (1) (1978) 104–105.
- [6] A.G. Imenes, D.R. Mills, Spectral beam splitting technology for increased conversion efficiency in solar concentrating systems: a review, *Solar Energy Materials and Solar Cells* 84 (1–4) (2004) 19–69.
- [7] Z.S. Chen, S.P. Mo, Z.H. Li, S.L. Jiang, B. Jiang, H.Q. Wang, B.L. Lu, Preliminary study of hybrid PV/thermal utilization of spectrum splitting solar energy, *Journal of Engineering Thermophysics* 29 (1) (2008) 13–15.
- [8] M. Brogren, A. Helgesson, B. Karlsson, J. Nilsson, A. Roos, Optical properties, durability, and system aspects of a new aluminium-polymer-laminated steel reflector for solar concentrators, *Solar Energy Materials and Solar Cells* 82 (3) (2004) 387–412.
- [9] C.G. Granqvist, Solar energy materials, *Advanced Materials* 15 (21) (2003) 1789–1803.
- [10] B.S. Negi, N.C. Bhowmik, T.C. Kandpal, Solar limb darkening and ray trace evaluation of solar concentrators, *Applied Optics* 24 (2) (1985) 296–299.
- [11] G. Johnston, Focal region measurements of the 20 m(2) tiled dish at the Australian National University, *Solar Energy* 63 (2) (1998) 117–124.
- [12] D. Riveros-Rosas, M. Sanchez-Gonzalez, C.A. Estrada, Three-dimensional analysis of a concentrated solar flux, *Journal of Solar Energy Engineering—Transactions of the ASME* 130 (1) (2008) 0145031–0145034.
- [13] Y. Shuai, X.L. Xia, H.P. Tan, Radiation performance of dish solar concentrator/cavity receiver systems, *Solar Energy* 82 (1) (2008) 13–21.
- [14] A. Luque, G. Sala, J.C. Arboiro, Electric and thermal model for non-uniformly illuminated concentration cells, *Solar Energy Materials and Solar Cells* 51 (3–4) (1998) 269–290.
- [15] J. Sun, T. Israeli, T.A. Reddy, K. Scoles, J.M. Gordon, D. Feuermann, Modeling and experimental evaluation of passive heat sinks for miniature high-flux photovoltaic concentrators, *Journal of Solar Energy Engineering—Transactions of the ASME* 127 (1) (2005) 138–145.
- [16] C. Gueymard, D. Myers, K. Emery, Proposed reference irradiance spectra for solar energy systems testing, *Solar Energy* 73 (6) (2002) 443–467.
- [17] M. Minnaert, The photosphere, in: G.P. Kuiper (Ed.), *The Sun, The Solar System* IUniversity of Chicago, Chicago, 1953.
- [18] A. Neumann, A. Witzke, S.A. Jones, G. Schmitt, Representative terrestrial solar brightness profiles, *Journal of Solar Energy Engineering—Transactions of the ASME* 124 (2) (2002) 198–204.
- [19] D. Buie, A.G. Monger, C.J. Dey, Sunshape distributions for terrestrial solar simulations, *Solar Energy* 74 (2) (2003) 113–122.
- [20] P.I. Cooper, The absorption of radiation in solar stills, *Solar Energy* 12 (3) (1969) 333–346.
- [21] A.G. Imenes, D. Buie, D. McKenzie, The design of broadband, wide-angle interference filters for solar concentrating systems, *Solar Energy Materials and Solar Cells* 90 (11) (2006) 1579–1606.
- [22] B.T. Sullivan, J.A. Dobrowolski, Implementation of a numerical needle method for thin-film design, *Applied Optics* 35 (28) (1996) 5484–5492.
- [23] A.V. Tikhonravov, M.K. Trubetskov, Application of the needle optimization technique to the design of optical coatings, *Applied Optics* 35 (28) (1996) 5493–5508.